

# Linearization of an Electron Beam's Longitudinal Phase Space Using a Hollow-Channel Plasma

Yipeng Wu<sup>1,\*,†</sup>, Zheng Zhou<sup>2,‡</sup>, Yingchao Du,<sup>2,†</sup> Jianfei Hua,<sup>2</sup> Wei Lu,<sup>2</sup> Warren B. Mori,<sup>1</sup> and Chan Joshi<sup>1</sup>

<sup>1</sup>University of California, Los Angeles, California 90095, USA

<sup>2</sup>Department of Engineering Physics, Tsinghua University, Beijing 100084, China



(Received 2 December 2022; revised 31 March 2023; accepted 4 May 2023; published 5 June 2023)

The removal of undesired beam nonlinear energy chirp (time-energy correlation) or linearization of the beam longitudinal phase space (LPS) is crucial for high-brightness linac-based scientific applications, such as x-ray free-electron lasers. In this paper, we propose that a low-density hollow channel plasma can be used as a near-ideal passive linearizer to significantly linearize the beam LPS and, at the same time, preserve the beam emittance. Physically, the passage of the beam through the hollow plasma channel excites a strong quasicosinoidal longitudinal wakefield that acts to mitigate the beam nonlinear energy chirp by superimposing a reverse chirp on the beam. The theoretical analyses and large-scale three-dimensional start-to-end simulations confirm that the beam longitudinal phase space can be almost completely linearized without noticeable beam emittance growth. Application of such a near-ideal linearizer may significantly improve the performance of numerous accelerator-based applications.

DOI: 10.1103/PhysRevApplied.19.064013

## I. INTRODUCTION

Accelerator-based applications, such as x-ray free-electron lasers (XFELs) [1–4] are revolutionizing science at ultrafast and ultrasmall scales. For these applications, precise control of the electron beam's longitudinal phase space (LPS) is critical. However, since the beam is usually generated and accelerated in a linac powered by rf waves, nonlinear energy chirp will be induced on the beam LPS due to the cosinoidal rf time curvature. This nonlinear energy chirp is normally detrimental to the application performance. For example, in XFELs, the nonlinear energy chirp results in the degradation of the FEL bandwidth. In addition, such a chirp will also cause unwanted deterioration of the bunch compression. In an XFEL, in order to achieve a high peak current for efficient lasing, the electron bunch generated in the linac needs to be temporally compressed by a magnetic chicane. However, the beam nonlinear energy chirp will strongly influence the final compression results, leading to sharp temporal spikes and unnecessary amplification of undesired collective effects. Therefore, removal of such nonlinear time-energy correlation or linearization of the beam LPS is highly desirable for improving the XFEL performance.

One typical method of eliminating the beam nonlinear energy chirp is the use of a high-harmonic cavity [5,6].

Nonlinear chirps can be compensated when the harmonic cavity is operated at a decelerating phase and proper voltage. However, this active compensation method requires an extra expensive rf station, as well as precise control of the amplitudes and phases of the rf structures. Moreover, the beam energy will also be reduced by approximately  $1/n^2$  during linearization, where  $n = k_h/k_a$  is the harmonic number, with  $k_h$  and  $k_a$  being the rf wave numbers of the high-harmonic cavity and main accelerating cavity, respectively. The beam LPS can also be linearized by shaping the photoinjector laser pulse [7]. Nevertheless, this method may increase the beam emittance. Another rf-free method is to exploit the interaction of the beam and its self-induced wakefield in accelerating sections and dielectric lined or corrugated metallic structures [8–12]. The planar structures are currently attracting considerable interest from most XFEL facilities because their gaps can be adjusted such that the wake wavelength can match the bunch length. However, the planar-structure geometry excites time-dependent quadrupole wakefields that can increase beam emittance even for an on-axis beam, which must be canceled by using two identical parts with orthogonal orientations [10].

An alternative, rf-free approach to tune the electron-beam LPS is to utilize the wakefield excited by either the electron beam itself (passive compensation) or an external laser or beam driver (active compensation) in a plasma [13–21]. Compared with the active compensation method, which requires additional high-power laser pulses or high-current particle beams [13–15], the passive

\*wuyipeng@ucla.edu

†dych@mail.tsinghua.edu.cn

‡These authors contributed equally to this work.

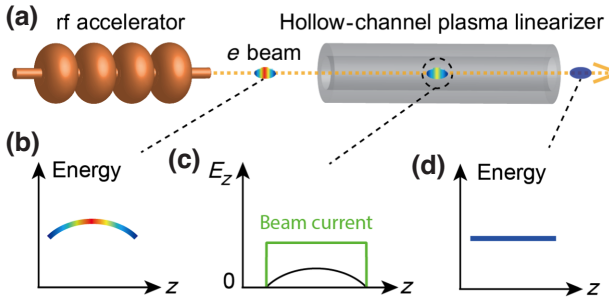


FIG. 1. (a) Schematic diagram of the hollow-channel plasma linearizer. (b) The initial beam LPS. (c) The beam current profile (green line) and the on-axis longitudinal wakefield  $E_z$  excited by the beam inside the hollow-channel plasma linearizer (black line). (d) The final beam LPS.

compensation scheme is simpler and easier to implement. Recently, both the passive dechirpers [16–18] and linearizers [19] based on tenuous uniform plasmas have been experimentally demonstrated to remove the linear and nonlinear energy chirps, respectively. However, this approach has a limitation for maintaining emittances well below about  $1 \mu\text{m rad}$  due to longitudinal-position-dependent transverse wakefield focusing. In addition, linearizing in a uniform plasma also induces slice energy-spread increase due to the nonuniform longitudinal wakefield in the transverse dimensions. These two factors impose restrictions for its application to XFELs. Ideally, a linearizer that can both remove the nonlinear energy chirp and maintain the emittance as well as the slice energy spread is preferred.

In this paper, we propose to use a low-density hollow-channel plasma to serve as a near-ideal linearizer, as shown in the schematic diagram in Fig. 1(a). We note that recent experiments have shown that such a hollow-channel plasma can be generated by ionizing neutral gas or alkali vapor with a high-order Bessel laser beam [22]. In our proposed scheme, an electron beam with a nonlinear energy chirp [Fig. 1(b)] is sent through a separate low-density hollow-channel plasma section to excite a strong quasi-cosinoidal longitudinal plasma wakefield [Fig. 1(c)]. By properly choosing the wavelength of the wakefield, the nonlinear energy chirp can be effectively canceled during the propagation [Fig. 1(d)]. The net linearizing effects can be easily tuned by changing the density, length, and geometry (i.e., inner and outer radii) of the plasma channel. Additionally, the transverse focusing fields inside the channel will be zero or negligibly small if the beam is launched on or very close to the axis, and this will help to preserve the beam emittance [23]. The transverse profile of the longitudinal field is also decoupled from the transverse profile of the electron beam [24]. Therefore, the longitudinal field inside the channel is uniform in the transverse direction, leading to zero slice-energy-spread increase.

This paper is organized as follows. In Secs. II and III, detailed theoretical analyses and start-to-end three-dimensional (3D) simulations will be systematically presented to show the effectiveness of the above scheme on nonlinear energy-chirp reduction and emittance preservation. In Sec. IV, we discuss the effect of the transverse dipole wakefield caused by the beam offset. Finally, we present concluding remarks in Sec. V.

## II. THEORETICAL ANALYSES

To quantify the effectiveness of the hollow-channel plasma linearizer, we first carry out a theoretical analysis based on the linear wakefield theory [24]. Typically, the electron beam before compression has relatively long pulse duration (ranging from picoseconds to tens of picoseconds) and relatively low current (ranging from amperes to tens of amperes). In this case, the linear wakefield theory can be adopted to properly describe the wakefield structure within the beam.

We begin by initializing a hollow-channel plasma with electron density  $n_p$  between the inner radius  $a$  and outer radius  $b$ . Using the linear wakefield theory, the longitudinal wakefield  $E_z$  in the hollow channel excited by an on-axis cylindrically symmetric beam can be expressed as a convolution of the bunch charge distribution with a single-particle wakefunction [22,24,25]

$$E_z(r, \xi) = E_p W_0 k_p \int_{-\infty}^{\xi} d\xi' \cos[\Omega_0 k_p (\xi - \xi')] I(\xi') / I_A, \quad (1)$$

where  $\xi = ct - z$  is the co-moving coordinate with the beam,  $k_p = \sqrt{n_p e^2 / m \epsilon_0 c^2}$  is the plasma wave number,  $E_p = m k_p c^2 / e$  is the wave-breaking limit of the cold plasma,  $I(\xi)$  is the beam current and  $I_A = mc^3/e \approx 17 \text{ kA}$  is the Alfvén current, with  $c$  the speed of light in vacuum,  $e$  the elementary charge,  $m$  the electron rest mass, and  $\epsilon_0$  the vacuum permittivity. In Eq. (1),  $W_0$  and  $\Omega_0$  are two quantities related to the wake amplitude and wavelength,

$$W_0 = \frac{-4B_{00}(a, b)}{k_p a [2B_{10}(a, b) - k_p a B_{00}(a, b)]}, \quad (2)$$

$$\Omega_0 = \sqrt{\frac{2B_{10}(a, b)}{2B_{10}(a, b) - k_p a B_{00}(a, b)}}, \quad (3)$$

where  $B_{ij}(a, b) = (-1)^{i-j+1} I_j(k_p b) K_i(k_p a) + I_i(k_p a) K_j(k_p b)$ , and  $K_n$  and  $I_n$  are the modified Bessel functions of order  $n$ .

For simplicity, we consider beams with flat-top current distributions [ $I(\xi) = I_b$  for  $-L_b/2 \leq \xi \leq L_b/2$ , where  $I_b$  is the beam peak current and  $L_b$  is the full bunch length]. Within the beam ( $-L_b/2 \leq \xi \leq L_b/2$ ), Eq. (1) can be

simplified as

$$E_z(r, \xi) = \frac{E_p W_0 I_b}{\Omega_0 I_A} \sin \left( \Omega_0 k_p \xi + \frac{\Omega_0 k_p L_b}{2} \right). \quad (4)$$

From Eq. (4), one can see that in order to effectively linearize the beam LPS,  $E_z$  along the electron beam should be a cosinoidal-waveform decelerating field with a wavelength near twice the bunch length, i.e.,  $\Omega_0 k_p L_b \approx \pi$ .

In this case, by considering an electron beam passing through  $n$  accelerating rf structures and then a hollow-channel plasma linearizer with length  $L_c$ , we present the beam LPS at the exit of the linearizer as

$$\begin{aligned} E(r, \xi) &= \sum_{i=1}^n E_{\text{acc},i} \cos(\phi_i + k_i \xi) - e E_z(r, \xi) L_c \\ &= - \sum_{i=1}^n E_{\text{acc},i} \sin \phi_i \sin k_i \xi \\ &\quad + \sum_{i=1}^n E_{\text{acc},i} \cos \phi_i \cos k_i \xi \\ &\quad - e \frac{E_p W_0 I_b}{\Omega_0 I_A} \cos(\Omega_0 k_p \xi) L_c, \end{aligned} \quad (5)$$

where  $E_{\text{acc},i}$  is the peak energy gain,  $k_i$  is the wave number, and  $\phi_i$  is the accelerating phase of the beam center (reference particle) in the  $i$ th rf structure. In the limit of  $k_i L_b \ll 1$ ,  $\sin k_i \xi \approx k_i \xi$ , and  $\cos k_i \xi \approx 1 - (k_i \xi)^2 / 2$ , thus the first term of Eq. (5) represents the linear energy chirp, the second term corresponds to the second-order energy chirp and the third term represents the energy chirp compensation due to the plasma linearizer. Under this condition, the nonlinear energy chirp can be almost canceled when

$$L_c = \frac{\sum_{i=1}^n E_{\text{acc},i} \cos \phi_i [1 - \cos(k_i L_b / 2)]}{e \frac{E_p W_0 I_b}{\Omega_0 I_A}}. \quad (6)$$

Therefore, the final LPS of this beam is given by

$$\begin{aligned} E_{\text{final}}(r, \xi) &= - \sum_{i=1}^n E_{\text{acc},i} \sin \phi_i \sin k_i \xi + \sum_{i=1}^n E_{\text{acc},i} \cos \phi_i \cos k_i \xi \\ &\quad - \sum_{i=1}^n E_{\text{acc},i} \cos \phi_i [1 - \cos(k_i L_b / 2)] \cos(\Omega_0 k_p \xi). \end{aligned} \quad (7)$$

To get an intuitive picture on the above physics, we plot in Fig. 2(a) the longitudinal field  $E_z$  excited by a 500-pC, 10-ps electron beam with a flat-top current profile ( $L_b = 3.0$  mm,  $I_b = 50$  A) inside a preformed annular plasma with an inner radius of  $a = 500$  μm and outer

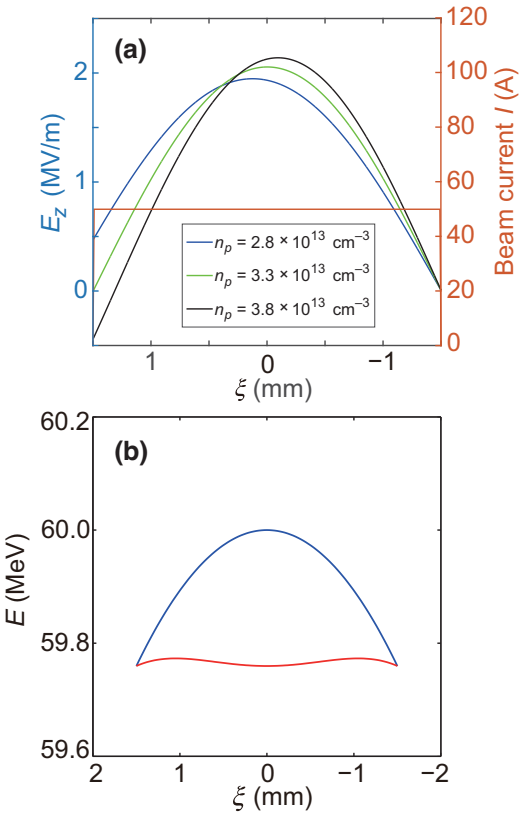


FIG. 2. (a) Longitudinal electric field  $E_z$  excited by a flat-top electron beam inside the hollow plasma channel, with plasma electron densities of  $2.8 \times 10^{13} \text{ cm}^{-3}$ ,  $3.3 \times 10^{13} \text{ cm}^{-3}$ , and  $3.8 \times 10^{13} \text{ cm}^{-3}$ , respectively. (b) LPS distributions of the electron beam, where the blue and red lines represent the LPS before and after the hollow-channel plasma linearizer, respectively, with the acceleration phase being  $0^\circ$ . Negative  $\xi$  corresponds to the head of the electron bunch.

radius of  $b = 1000$  μm. Three cases with plasma electron densities of  $2.8 \times 10^{13} \text{ cm}^{-3}$ ,  $3.3 \times 10^{13} \text{ cm}^{-3}$ , and  $3.8 \times 10^{13} \text{ cm}^{-3}$  are considered here. In the case of  $n_p = 3.3 \times 10^{13} \text{ cm}^{-3}$ , the relation  $\Omega_0 k_p L_b \approx \pi$  ( $\Omega_0 = 0.96$ ) is satisfied, and the corresponding LPS of this beam before and after the hollow-channel plasma linearizer is presented in Fig. 2(b). Here the electron beam is initially on-crest ( $\phi = 0^\circ$ ) accelerated in one S-band rf structure with frequency at 2856 MHz ( $k = 59.8 \text{ m}^{-1}$ ) and peak energy gain of  $E_{\text{acc}} = 60$  MeV. The nonlinear energy chirp of the electron beam induced by the rf curvature is nearly canceled by the plasma linearizer with a length of  $L_c = 12$  cm [calculated according to Eq. (6)]. The LPS after the plasma linearizer is not perfectly flat owing to the residual higher-order energy chirps. The reason is that the first and second terms in Eq. (7) correspond to the energy gain from the linac, which can be expanded only up to the second order in  $\xi$  by assuming that  $k_i L_b \ll 1$ , while the third term corresponding to the energy change from the plasma linearizer should be expanded to at least the fourth or even higher

order in  $\xi$  because  $\Omega_0 k_p L_b = \pi$ . In spite of this slight imperfection, the projected beam energy spread remains dramatically suppressed by at least one order of magnitude.

Furthermore, while propagating in the channel, a well-centered radial-symmetric relativistic electron beam does not experience a transverse wakefield. Given the absence of the plasma focusing force, the transverse particle momentum remains invariant and the beam emittance evolution during the linearizing process is the same as that in free-space drifting under the assumption that the change in the beam energy spread is negligible (this condition can easily be satisfied if the energy spread induced by the linear energy chirp is much larger than that induced by the nonlinear energy chirp). The geometric emittance

$\epsilon_{\text{geo}}$  ( $\epsilon_{\text{geo}} = 1/mc\sqrt{\langle x^2 \rangle \langle x'^2 \rangle - \langle xx' \rangle}$ , where  $\langle \rangle$  represents an ensemble average over the beam distribution,  $x$  is the transverse particle position, and  $x' = p_x/p_z$  is the slope of a particle trajectory, with  $p_x$  and  $p_z$  being the transverse and longitudinal particle momentum, respectively) remains invariant and the normalized emittance  $\epsilon_n$  ( $\epsilon_n = 1/mc\sqrt{\langle x^2 \rangle \langle p_x^2 \rangle - \langle xp_x \rangle}$ ) increases as

$$\epsilon_n(z) \approx \langle p_z \rangle \epsilon_{\text{geo}} \sqrt{\delta_E^2[(\gamma_{\text{init}} z - \alpha_{\text{init}})^2 + 1] + 1}, \quad (8)$$

where  $\delta_E = \sqrt{\langle p_z^2 \rangle - \langle p_z \rangle^2} / \langle p_z \rangle$  is the relative energy spread of the beam,  $\alpha$  and  $\gamma$  are the Twiss parameters, with  $\alpha = -\langle xx' \rangle / \epsilon_{\text{geo}}$  being the correlation between  $x$  and  $x'$  and  $\gamma = \langle x'^2 \rangle / \epsilon_{\text{geo}}$  being a measure of the spread in the particle slopes [26–28]. Here the subscript “init” refers to the initial quantity. For the typical parameters of the electron beam before compression from a linac-driven high-gain XFEL injector (e.g.,  $\langle p_z \rangle = 400$  mc,  $\delta_E = 0.015$ ,  $\alpha_{\text{init}} = 0$ ,  $\epsilon_{\text{geo}} = 2.0$  nm.rad,  $\gamma_{\text{init}} = 1.5$  m $^{-1}$ ), the normalized emittance grows by 0.04% of the initial value after the electron beam passes through a 1-m-long plasma channel, which is extremely small and can be neglected.

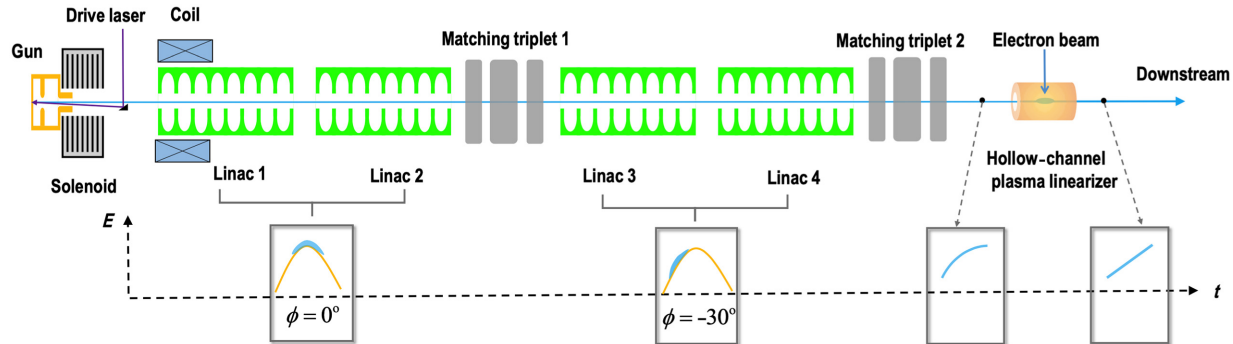


FIG. 3. Schematic of the beamline.

### III. START-TO-END SIMULATIONS

To further verify the validity of the hollow-channel plasma linearizer scheme and examine the theoretical results, practical start-to-end 3D simulations are performed. As shown in Fig. 3, the beamline used in the simulations consists of a photoinjector and a hollow-channel plasma linearizer. The beam generation and transport in the photoinjector comprising a photocathode rf gun and four accelerating linacs are simulated with the particle-tracking code ASTRA [29]. The simulations of beam passing through the hollow-channel plasma linearizer are implemented with the code OSIRIS, which is a fully parallelized, fully electromagnetic, and fully relativistic 3D particle-in-cell (PIC) code [30–32].

An electron beam with a near flat-top current distribution is required for the acquisition of optimized bunch emittance in the photocathode rf gun [33,34] and can be achieved by shaping the temporal distribution of the driving UV (266-nm) laser to a flat-top pulse through the pulse-stacking technique [35,36]. This flat-top beam current distribution is also preferred by hollow-channel plasma linearizers for the effective cancelation of the nonlinear energy chirp as mentioned above. In the simulation, the FWHM duration of the shaped driving UV laser is set to 10 ps, with a 9.3-ps-long flat-top distribution in the center and two 0.7-ps-long sharp rising and falling edges. The transverse distribution of the driving laser is uniform, and the laser-beam radius is 1.0 mm. The 1.6 cell S-band photocathode rf gun functions at a gradient of 100 MV/m, and the launching phase is set to 26°. A solenoid adjacent to the gun is used for the emittance compensation process [37,38]. The accelerating part is composed of four S-band accelerating structures, based on the model of standard SLAC 3-m traveling-wave accelerating sections. The maximum energy gain of each accelerating section is  $E_{\text{acc}} = 60$  MeV. The electron bunch is accelerated on crest in the first two linacs (i.e.,  $\phi_{1,2} = 0^\circ$ ) to gain energy, while it is  $-30^\circ$  off-crest accelerated in the following two linacs (i.e.,  $\phi_{3,4} = -30^\circ$ ) to obtain a linear energy chirp where the tail of the bunch has a higher energy than the head.

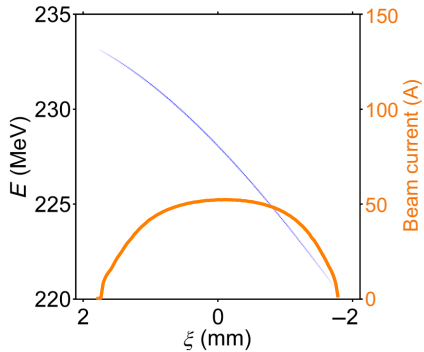


FIG. 4. LPS distribution (blue) and current profile (yellow) of the electron beam after the photoinjector.

This linear energy chirp is required by the chicane compressor to longitudinally compress the beam to achieve high current. At the exit of Linac 4, an electron bunch with a mean energy of 227.3 MeV, charge of 500 pC, full bunch length of 3.45 mm (FWHM bunch length of 2.94 mm), and low normalized emittance of 0.82  $\mu\text{m}$  rad is obtained. The beam LPS and current profile are plotted in Fig. 4. Due to the relatively long bunch length, which spans over 10° accelerating phase of the rf wavelength, unwanted nonlinear time-energy correlation is added to the desired linear energy chirp (see Fig. 4). The electron beam is then focused to a transverse waist size of 21  $\mu\text{m}$  (see Fig. 5) in the middle of the hollow plasma channel by the matching triplets. Detailed parameters of the electron bunch are listed in Table I.

The linearizing process is simulated using the 3D PIC code OSIRIS in Cartesian coordinates with a window moving at the speed of light. To control and eliminate the numerical Cerenkov instability [39,40], we adopt a customized finite-difference-time-domain Maxwell solver for the PIC algorithm as addressed in Ref. [41]. The 3600  $\times$

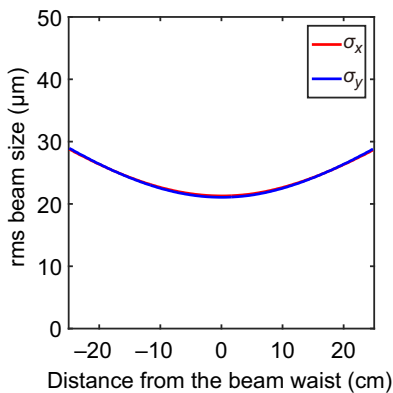


FIG. 5. Simulated evolution of the beam rms transverse size (focused by the matching triplets) inside the hollow-channel plasma linearizer. Here the beam waist is located in the middle of the hollow plasma channel.

TABLE I. Beam parameters at the exit of the photoinjector.

Parameter	Value
Charge $Q$	500 pC
Full bunch length $L_b$	3.45 mm (11.5 ps)
FWHM bunch length $L_{b,\text{FWHM}}$	2.94 mm (9.8 ps)
Mean beam current $I_{b,\text{mean}} = Q/L_{b,\text{FWHM}}$	51 A
rms beam waist size $\sigma_{x,y}$	21 $\mu\text{m}$
Mean energy $E_{\text{mean}}$	227.3 MeV
rms energy spread $\Delta_E$	3.1 MeV
rms slice energy spread $\Delta_{E,\text{slice}}$	1.0 keV
Normalized emittance $\epsilon_n$	0.82 $\mu\text{m}$ rad

3000  $\times$  3000  $\mu\text{m}^3$  simulation window is divided into 1500  $\times$  1000  $\times$  1000 cells along the  $z$ ,  $x$ , and  $y$  directions, respectively. A preformed fully ionized hollow plasma channel is initialized with an electron density of  $n_p = 2.5 \times 10^{13} \text{ cm}^{-3}$  between the inner radius of  $a = 500 \mu\text{m}$  and outer radius of  $b = 1000 \mu\text{m}$ , which satisfy the relation  $\Omega_0 k_p L_b \approx \pi$  ( $\Omega_0 = 0.96$ ). A neutralizing immobile ion background is used. The hollow-channel plasma and the electron beam are represented by 8 and 16 particles per cell, respectively.

The simulation results are shown in Fig. 6. The densities of the electron beam and the hollow-channel plasma are shown in Fig. 6(a). Figure 6(b) presents the  $E_z$  field excited by this electron beam in the hollow plasma channel. The on-axis lineout (black solid line) shows that  $E_z$  within the beam is a quasicosine waveform decelerating field with a wavelength that is approximately twice the full bunch length and an amplitude (the maximum decelerating gradient) of 2 MV/m. For comparison, the  $E_z$  field obtained through theoretical calculation [according to Eq. (1)] is also presented in this figure (black dashed line) and is in excellent agreement with the simulation result. The transverse variation of  $E_z$  (red solid line) shows that  $E_z$  is uniform along the transverse dimension inside the channel. Given these two properties of  $E_z$ , the beam can be linearized in the hollow plasma channel without inducing slice energy-spread increase. The corresponding beam LPS at the exit of the hollow-channel plasma linearizer with different channel lengths are shown in Fig. 6(c). As a comparison, the LPS before the linearizer is also added in this figure. The nonlinear energy chirp of the electron beam can be almost fully canceled for  $L_c = 51 \text{ cm}$ . The simulation result of this optimal linearizer length value is reasonably in agreement with the theoretical calculation according to Eq. (6) where  $L_c = \sum_{i=1}^4 E_{\text{acc},i} \cos \phi_i [1 - \cos(k_i L_b / 2)] / e(E_p W_0 / \Omega_0) (I_{b,\text{mean}} / I_A) \approx 60 \text{ cm}$  by assuming that the wakefield amplitude in this case is nearly equal to that excited by a flat-top beam with a bunch length of  $L_{b,\text{FWHM}}$  and beam current of  $I_{b,\text{mean}}$ . When the hollow-channel plasma linearizer is longer than this optimal value (e.g.,  $L_c = 75 \text{ cm}$ ), the nonlinear energy

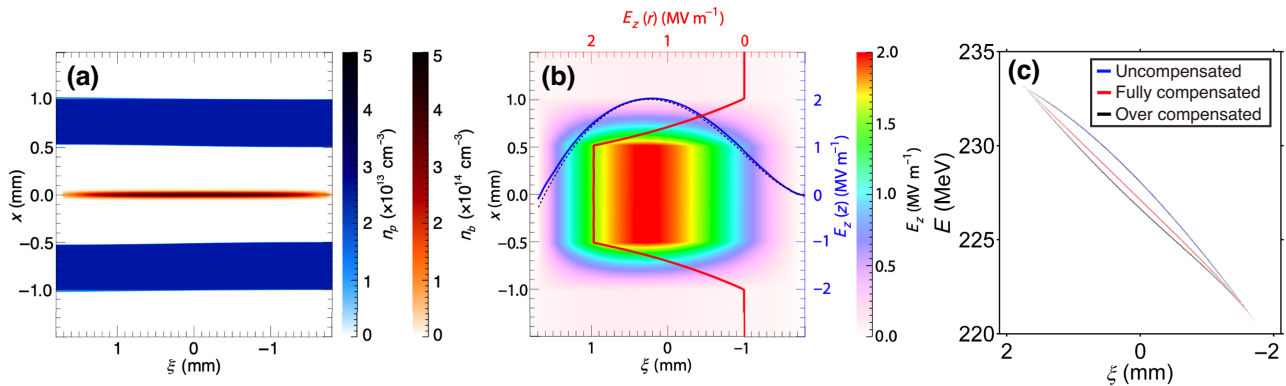


FIG. 6. 3D PIC simulations of the linearizing process in a hollow-channel plasma. (a) Densities of the plasma channel and the electron beam. (b) Longitudinal field  $E_z$  excited by the electron beam. Lineouts of the simulated and calculated [according to Eq. (1)]  $E_z$  field ( $x = 0 \mu\text{m}$ ,  $\xi$ ) are shown with solid and dashed black lines, respectively. The red solid line shows the transverse variation in  $E_z$  at  $\xi = 0 \text{ mm}$ . (c) LPS distributions of the electron beam, where the blue color represents the LPS before the plasma linearizer (nonlinear energy chirp uncompensated), while the red and black colors represent the LPS after the linearizer with  $L_c$  of 51 cm (nonlinear energy chirp fully compensated) and 75 cm (nonlinear energy chirp overcompensated), respectively.

chirp may be overcompensated [see the black line in Fig. 6(c)]. As addressed above, owing to the absence of the plasma-focusing force, the evolution of beam emittance is similar to that in free-space drifting. The geometrical emittance  $\epsilon_{\text{geo}}$  remains invariant, and the normalized emittance  $\epsilon_n$  also remains nearly constant during the linearizing process, as shown in Fig. 7 (blue line). This property of maintaining low emittance is crucial for XFELs to achieve high performance. For comparison, we also simulate the linearizing process of the same electron beam in a uniform plasma with a density identical to that in the above simulation. Due to longitudinal-position-dependent transverse wakefield, electrons at different longitudinal positions feel different focusing strengths and rotate with different velocities in the transverse phase space, leading to a large growth

in projected emittance. In Fig. 7, the evolution of the beam normalized emittance over the whole propagation is also plotted (red line), and it is clear that the emittance increases by a factor of 2. Such a large emittance growth is likely unacceptable for XFEL applications of the beam.

To quantitatively compare the nonlinear energy chirp before and after the hollow channel plasma linearizer, the energy chirp is fitted with a fifth-order polynomial function (the convergence of the fitting has been confirmed). Since the linearizer is mainly used to compensate for the second-order energy chirp, we evaluate the linearizing effect by comparing the second-order coefficient  $c_2$  of the polynomial function. Figure 8(a) plots the evolution of the second-order chirp coefficient  $c_2$  versus the plasma length  $L_c$  for different plasma-density values of  $n_p = 2.0 \times 10^{13} \text{ cm}^{-3}$ ,  $2.5 \times 10^{13} \text{ cm}^{-3}$ , and  $3.0 \times 10^{13} \text{ cm}^{-3}$ , respectively. Note that the case with  $n_p = 2.5 \times 10^{13} \text{ cm}^{-3}$  corresponds to the simulation in Fig. 6. As one can see,  $c_2$  linearly decreases to zero and then changes sign as the beam propagates in the channel. This linear dependence can be easily explained via a simple Taylor expansion of Eq. (5). The change rates of  $c_2$  versus  $L_c$  are different for different density values, where the highest  $n_p$  [ $3.0 \times 10^{13} \text{ cm}^{-3}$ , see the black dotted line in Fig. 8(a)] corresponds to the largest change rate and vice versa.

Although the second-order chirp can be canceled in all three density cases, the residual higher-order nonlinear chirp can be different. Figure 8(b) shows the beam LPS with the initial linear energy chirp subtracted. In the case of  $n_p = 2.5 \times 10^{13} \text{ cm}^{-3}$  where the relation  $\Omega_0 k_p L_b \approx \pi$  is satisfied, the longitudinal field  $E_z$  excited by the beam is zero at the bunch head and bunch tail; thus the energy values of these two parts remain nearly unchanged during the linearizing process. However, given that the current distribution is not ideally flat top,  $E_z$  is an imperfect cosine

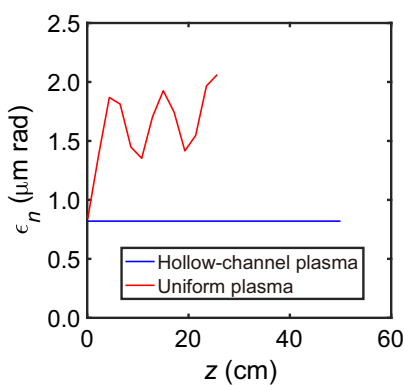


FIG. 7. Evolutions of beam normalized emittance during the linearizing process in both the hollow-channel plasma (blue) and the uniform plasma (red). Note that in the uniform plasma linearizer case, due to the stronger  $E_z$  field, the required plasma length is shorter than that in the corresponding hollow-channel plasma linearizer case.

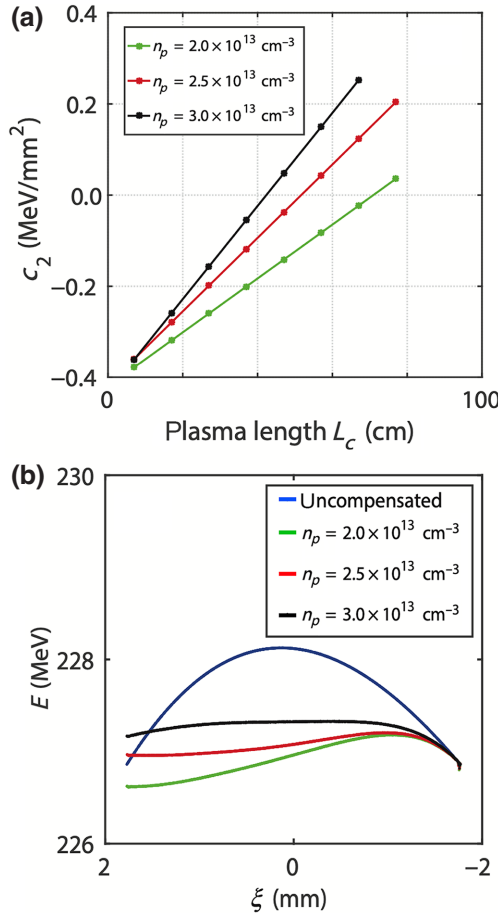


FIG. 8. Outcome of the linearizing process with different plasma densities. (a) Change of the second-order coefficient  $c_2$  as a function of plasma length  $L_c$ . (b) Beam LPS with the initial linear chirp subtracted.

function and does not reach its peak at the beam center [see Fig. 6(b)]. Thus, higher-order nonlinear energy chirp is introduced. In the case of a lower plasma density ( $n_p = 2.0 \times 10^{13} \text{ cm}^{-3}$ ), the wakefield wavelength increases and thus the bunch tail loses energy. In addition, the peak position of  $E_z$  is shifted farther from the beam center, thereby increasing the residual higher-order energy chirp. Conversely, the bunch tail gains energy and the residual higher-order energy chirp decreases at a higher plasma density ( $n_p = 3.0 \times 10^{13} \text{ cm}^{-3}$ ). Despite these small differences in the linearizing results for different plasma densities, Fig. 8 presents an encouraging result that the hollow channel plasma linearizer functions well at a relatively wide range of plasma densities, showing the practical applicability of this linearizing technique.

#### IV. INFLUENCE OF THE DIPOLE WAKEFIELD INDUCED BY BEAM OFFSET

In this section, we discuss the transverse wakefield that can be generated in the plasma linearizer when the electron

beam enters the channel offset from the axis. We are particularly interested in the fields associated with the dipole mode, which is the strongest mode contributing to the transverse beam break-up instability [25,42,43]. The wake function can be calculated as shown in Ref. [25] based on the linear theory, and by convolving the wake function with the beam current distribution, we can obtain the transverse wakefield  $W_\perp = E_r - cB_\theta$  experienced by the electron beam with offset  $x_0$  (assuming in the  $x$  direction)

$$W_\perp(\xi) = E_p W_1 x_0 k_p^2 \int_{-\infty}^{\xi} d\xi' \sin[\Omega_1 k_p(\xi - \xi')] I(\xi') / I_A, \quad (9)$$

where

$$W_1 = \frac{8B_{11}(a, b)}{\Omega_1(k_p a)^3 [4B_{21}(a, b) - k_p a B_{11}(a, b)]}, \quad (10)$$

$$\Omega_1 = \sqrt{\frac{2B_{21}(a, b)}{4B_{21}(a, b) - k_p a B_{11}(a, b)}}. \quad (11)$$

For the flat-top current distribution mentioned above, Eq. (9) is reduced to

$$W_\perp(\xi) = \frac{E_p W_1}{\Omega_1} \frac{I_b}{I_A} k_p x_0 \left[ 1 - \cos \left( \Omega_1 k_p \xi + \frac{\Omega_1 k_p L_b}{2} \right) \right]. \quad (12)$$

The transverse dipole wakefield is constant inside the channel and points in the same direction as the beam offset, away from the axis. The strength of the wake scales linearly with the beam offset  $x_0$ . The beam should be kept as close to the axis as possible to mitigate the effect of the transverse wakefield. Figure 9(a) shows the comparison of the transverse dipole wakefield  $W_\perp$  inside the channel from the 3D PIC simulation and theoretical calculation with the beam offset  $x_0 = 3 \mu\text{m}$ . The beam and plasma parameters in this simulation and all following simulations are identical to those in Fig. 6. Good agreement is achieved between the simulated and theoretical results. The  $W_\perp$  also has a longitudinal dependence of the beam position, thus in the beam transverse phase space, slice phase ellipses develop a displacement with respect to each other, which leads to the projected emittance growth. Figure 9(b) shows the transverse beam offset growth and the relative beam projected emittance growth (in the direction of the offset) versus the initial beam offset. As one can see, the beam offset growth is negligibly small compared to the channel inner radius  $a$ , and the beam emittance growth can be controlled to less than approximately 25% for initial beam offset within 4  $\mu\text{m}$ . This tolerance can be achieved for the XFEL beam conditions and current diagnostics. Furthermore, this initial offset value has minimal impact on the beam propagation and linearizing results.

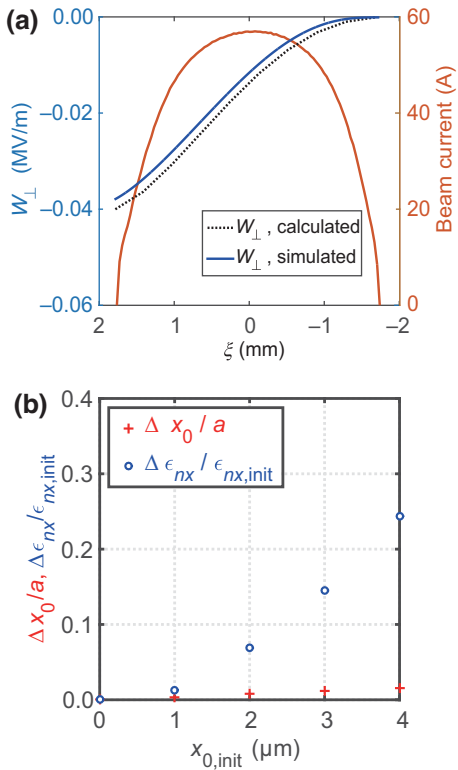


FIG. 9. (a) Simulated (solid blue) and calculated (dotted black) on-axis transverse dipole wakefield with the beam offset  $x_0 = 3 \mu\text{m}$ . The beam current profile is also shown with the solid brown line. (b) The transverse offset growth of the beam centroid  $\Delta x_0/a$  and the the projected normalized emittance growth  $\Delta \epsilon_{nx}/\epsilon_{nx,init}$  versus the initial beam offset  $x_{0,init}$ . Here  $\Delta x_0 = x_{0,\text{final}} - x_{0,\text{init}}$  and  $\Delta \epsilon_{nx} = \epsilon_{nx,\text{final}} - \epsilon_{nx,\text{init}}$ , where the subscripts “init” and “final” denote the initial and final quantities, respectively.

## V. CONCLUSION

The proposed method can also be easily utilized for the linearization of shorter beams typically used in compact scientific facilities that employ  $X$  band (frequency approximately 12 GHz) linacs. In that case, an active compensation scheme with a harmonic cavity at even higher frequency becomes extremely difficult for the lack of a suitable high-power rf source. Utilizing dielectric lined or corrugated metallic structures requires very small geometric parameters to match the short bunch duration, bringing difficulty to structure manufacturing and beam alignment. By contrast, generating an annular plasma with a relatively high density, short length can be readily achieved, therefore using a hollow-channel plasma linearizer to remove the beam nonlinear energy spread is properly a highly attractive method.

In summary, an alternative method that uses a hollow-channel plasma as a near-ideal linearizer to mitigate the beam nonlinear energy chirp is proposed. Theoretical analyses and start-to-end 3D simulations are systematically

used to confirm the effectiveness and robustness of this method for linearizing the beam LPS, while maintaining the beam slice energy spread and normalized emittance. This tunable and flexible technique can be applied to numerous accelerator-based scientific facilities for significantly enhancing the beam quality. Since the generation of a hollow plasma channel has already been demonstrated [22], the proposed method can be experimentally tested in the near future.

## ACKNOWLEDGMENTS

Yipeng Wu and Zheng Zhou contributed equally to this work.

This work is supported by the National Natural Science Foundation of China (NSFC) (Grants No. 11535006, No. 11991071, No. 11775125, and No. 11875175), the CAS Center for Excellence in Particle Physics, the U.S. Department of Energy (Grants No. DE-SC0010064), and the U.S. National Science Foundation (NSF) (Grant No. 1734315). The simulations are performed on Cori cluster at National Energy Research Scientific Computing Center (NERSC).

- [1] B. W. J. McNeil and N. R. Thompson, X-ray free-electron lasers, *Nat. Photonics* **4**, 814 (2010).
- [2] Z. T. Zhao, D. Wang, J. H. Chen, Z. H. Chen, H. X. Deng, J. G. Ding, C. Feng, Q. Gu, M. M. Huang, and T. H. Lan, *et al.*, First lasing of an echo-enabled harmonic generation free-electron laser, *Nat. Photonics* **6**, 360 (2012).
- [3] J. Amann, W. Berg, V. Blank, F.-J. Decker, Y. Ding, P. Emma, Y. Feng, J. Frisch, D. Fritz, and J. Hastings, *et al.*, Demonstration of self-seeding in a hard-x-ray free-electron laser, *Nat. Photonics* **6**, 693 (2012).
- [4] E. Allaria, D. Castronovo, P. Cinquegrana, P. Craievich, M. D. Forno, M. B. Danailov, G. D'Auria, A. Demidovich, G. D. Ninno, and S. D. Mitri, *et al.*, Two-stage seeded soft-x-ray free-electron laser, *Nat. Photonics* **7**, 913 (2013).
- [5] P. Emma, X-band rf harmonic compensation for linear bunch compression in the lcls, SLAC, Stanford, CA, USA, Rep. LCLS-TN-01-1. (2001).
- [6] J. Arthur, P. Anfinrud, P. Audebert, K. Bane, I. Ben-Zvi, V. Bharadwaj, R. Bionta, P. Bolton, M. Borland, and P. H. Bucksbaum, *et al.*, Linac coherent light source (LCLS) conceptual design report, Tech. Rep. (2002).
- [7] G. Penco, M. Danailov, A. Demidovich, E. Allaria, G. De Ninno, S. Di Mitri, W. M. Fawley, E. Ferrari, L. Giannessi, and M. Trovó, Experimental Demonstration of Electron Longitudinal-Phase-Space Linearization by Shaping the Photoinjector Laser Pulse, *Phys. Rev. Lett.* **112**, 044801 (2014).
- [8] P. Craievich, Passive longitudinal phase space linearizer, *Phys. Rev. Spec. Top. Accel. Beams* **13**, 034401 (2010).
- [9] H. Deng, M. Zhang, C. Feng, T. Zhang, X. Wang, T. Lan, L. Feng, W. Zhang, X. Liu, and H. Yao, *et al.*, Experimental Demonstration of Longitudinal Beam Phase-Space

- Linearizer in a Free-Electron Laser Facility by Corrugated Structures, *Phys. Rev. Lett.* **113**, 254802 (2014).
- [10] F. Fu, R. Wang, P. Zhu, L. Zhao, T. Jiang, C. Lu, S. Liu, L. Shi, L. Yan, and H. Deng, *et al.*, Demonstration of Nonlinear-Energy-Spread Compensation in Relativistic Electron Bunches with Corrugated Structures, *Phys. Rev. Lett.* **114**, 114801 (2015).
- [11] A. Novokhatski, Wakefield potentials of corrugated structures, *Phys. Rev. Spec. Top. Accel. Beams* **18**, 104402 (2015).
- [12] G. Penco, E. Allaria, I. Cudin, S. D. Mitri, D. Gauthier, S. Spampinati, M. Trovó, L. Giannessi, E. Roussel, and S. Betttoni, *et al.*, Passive Linearization of the Magnetic Bunch Compression using Self-Induced Fields, *Phys. Rev. Lett.* **119**, 184802 (2017).
- [13] A. Döpp, C. Thaury, E. Guillaume, F. Massimo, A. Lifschitz, I. Andriyash, J.-P. Goddet, A. Tazfi, K. Ta Phuoc, and V. Malka, Energy-Chirp Compensation in a Laser Wakefield Accelerator, *Phys. Rev. Lett.* **121**, 074802 (2018).
- [14] R. Pompili, D. Alesini, M. P. Anania, M. Behtouei, M. Bellaveglia, A. Biagioni, F. G. Bisesto, M. Cesarini, E. Chiadroni, and A. Cianchi, *et al.*, Energy spread minimization in a beam-driven plasma wakefield accelerator, *Nat. Phys.* **17**, 499 (2021).
- [15] A. Ferran Pousa, I. Agapov, S. A. Antipov, R. W. Assmann, R. Brinkmann, S. Jalas, M. Kirchen, W. P. Leemans, A. R. Maier, and M. de la Ossa, *et al.*, Energy Compression and Stabilization of Laser-Plasma Accelerators, *Phys. Rev. Lett.* **129**, 094801 (2022).
- [16] Y. P. Wu, J. F. Hua, Z. Zhou, J. Zhang, S. Liu, B. Peng, Y. Fang, Z. Nie, X. N. Ning, and C.-H. Pai, *et al.*, Phase Space Dynamics of a Plasma Wakefield Dechirper for Energy Spread—Reduction, *Phys. Rev. Lett.* **122**, 204804 (2019).
- [17] R. D'Arcy, S. Wesch, A. Aschikhin, S. Bohlen, C. Behrens, M. J. Garland, L. Goldberg, P. Gonzalez, A. Knetsch, and V. Libov, *et al.*, Tunable Plasma-Based Energy Dechirper, *Phys. Rev. Lett.* **122**, 034801 (2019).
- [18] V. Shpakov, M. P. Anania, M. Bellaveglia, A. Biagioni, F. Bisesto, F. Cardelli, M. Cesarini, E. Chiadroni, A. Cianchi, and G. Costa, *et al.*, Longitudinal Phase-Space Manipulation with Beam-Driven Wakefields, *Phys. Rev. Lett.* **122**, 114801 (2019).
- [19] Y. Wu, J. Hua, Z. Zhou, J. Zhang, S. Liu, B. Peng, Y. Fang, X. Ning, Z. Nie, and Q. Tian, *et al.*, Tunable Plasma Linearizer for Compensation of Nonlinear Energy Chirp, *Phys. Rev. Appl.* **16**, 024056 (2021).
- [20] Y. Wu, J. Hua, C.-H. Pai, W. An, Z. Zhou, J. Zhang, S. Liu, B. Peng, Y. Fang, and S. Zhou, *et al.*, Near-Ideal Dechirper for Plasma-Based Electron and Positron Acceleration using a Hollow Channel Plasma, *Phys. Rev. Appl.* **12**, 064011 (2019).
- [21] H. Feng, Z. Zhou, Y. Wu, Z. Gao, Y. Liang, N. Huang, L. Yan, H. Deng, Y. Du, and R. Li, *et al.*, Generation of Tunable 10-mJ-Level Terahertz Pulses Through Nonlinear Plasma Wakefield Modulation, *Phys. Rev. Appl.* **15**, 044032 (2021).
- [22] S. Gessner, E. Adli, J. M. Allen, W. An, C. I. Clarke, C. E. Clayton, S. Corde, J. P. Delahaye, J. Frederico, and S. Z. Green, *et al.*, Demonstration of a positron beam-driven hollow channel plasma wakefield accelerator, *Nat. Commun.* **7**, 11785 (2016).
- [23] T. C. Chiou and T. Katsouleas, High Beam Quality and Efficiency in Plasma-Based Accelerators, *Phys. Rev. Lett.* **81**, 3411 (1998).
- [24] C. B. Schroeder, D. H. Whittum, and J. S. Wurtele, Multimode Analysis of the Hollow Plasma Channel Wakefield Accelerator, *Phys. Rev. Lett.* **82**, 1177 (1999).
- [25] S. Gessner, Ph.D. thesis, Stanford University, 2016.
- [26] P. Antici, A. Bacci, C. Benedetti, E. Chiadroni, M. Ferrario, A. R. Rossi, L. Lancia, M. Migliorati, A. Mostacci, and L. Palumbo, *et al.*, Laser-driven electron beamlines generated by coupling laser-plasma sources with conventional transport systems, *J. Appl. Phys.* **112**, 044902 (2012).
- [27] M. Migliorati, A. Bacci, C. Benedetti, E. Chiadroni, M. Ferrario, A. Mostacci, L. Palumbo, A. R. Rossi, L. Serafini, and P. Antici, Intrinsic normalized emittance growth in laser-driven electron accelerators, *Phys. Rev. Spec. Top. Accel. Beams* **16**, 011302 (2013).
- [28] X. L. Xu, J. F. Hua, Y. P. Wu, C. J. Zhang, F. Li, Y. Wan, C.-H. Pai, W. Lu, W. An, and P. Yu, *et al.*, Physics of Phase Space Matching for Staging Plasma and Traditional Accelerator Components Using Longitudinally Tailored Plasma Profiles, *Phys. Rev. Lett.* **116**, 124801 (2016).
- [29] K. Flottmann, Astra user manual, ASTRA User Manual, <http://www.desy.de/mypyflo>.
- [30] R. A. Fonseca, L. O. Silva, F. S. Tsung, V. K. Decyk, W. Lu, C. Ren, W. B. Mori, S. Deng, S. Lee, and T. Katsouleas, *et al.*, Osiris: A three-dimensional, fully relativistic particle in cell code for modeling plasma based accelerators, *Lect. Notes Comput. Sci.* **2331**, 342 (2002).
- [31] R. A. Fonseca, S. F. Martins, L. O. Silva, J. W. Tonge, F. S. Tsung, and W. B. Mori, One-to-one direct modeling of experiments and astrophysical scenarios: Pushing the envelope on kinetic plasma simulations, *Plasma Phys. Control. Fusion* **50**, 124034 (2008).
- [32] R. A. Fonseca, J. Vieira, F. Fiúza, A. Davidson, F. S. Tsung, W. B. Mori, and L. O. Silva, Exploiting multi-scale parallelism for large scale numerical modelling of laser wakefield accelerators, *Plasma Phys. Control. Fusion* **55**, 124011 (2013).
- [33] J. Yang, F. Sakai, T. Yanagida, M. Yorozu, Y. Okada, K. Takasago, A. Endo, A. Yada, and M. Washio, Low-emittance electron-beam generation with laser pulse shaping in photocathode radio-frequency gun, *J. Appl. Phys.* **92**, 1608 (2002).
- [34] L. Zheng, Y. Du, Z. Zhang, H. Qian, L. Yan, J. Shi, Z. Zhang, Z. Zhou, X. Wu, and X. Su, *et al.*, Development of S-band photocathode rf guns at Tsinghua University, *Nucl. Instrum. Methods Phys. Res., Sect. A* **834**, 98 (2016).
- [35] L. Yan, Q. Du, Y. Du, J. Hua, W. Huang, and C. Tang, UV pulse shaping for the photocathode rf gun, *Nucl. Instrum. Methods Phys. Res., Sect. A* **637**, S127 (2011).
- [36] J. G. Power and C. Jing, in *AIP Conference Proceedings*, Vol. 1086 (AIP, Santa Cruz, California, USA, 2009), p. 689.
- [37] B. E. Carlsten, New photoelectric injector design for the Los Alamos National Laboratory XUV FEL accelerator, *Nucl. Instrum. Methods Phys. Res., Sect. A* **285**, 313 (1989).
- [38] L. Serafini and J. B. Rosenzweig, Envelope analysis of intense relativistic quasilaminar beams in rf photoinjectors:

- Ma theory of emittance compensation, *Phys. Rev. E* **55**, 7565 (1997).
- [39] B. B. Godfrey and J.-L. Vay, Numerical stability of relativistic beam multidimensional PIC simulations employing the Esirkepov algorithm, *J. Comput. Phys.* **248**, 33 (2013).
- [40] X. Xu, P. Yu, S. F. Martins, F. S. Tsung, V. K. Decyk, J. Vieira, R. A. Fonseca, W. Lu, L. O. Silva, and W. B. Mori, Numerical instability due to relativistic plasma drift in EM-PIC simulations, *Comput. Phys. Commun.* **184**, 2503 (2013).
- [41] F. Li, P. Yu, X. Xu, F. Fiuzza, V. K. Decyk, T. Dalichaouch, A. Davidson, A. Tableman, W. An, and F. S. Tsung, *et al.*, Controlling the numerical Cerenkov instability in PIC simulations using a customized finite difference Maxwell solver and a local FFT based current correction, *Comput. Phys. Commun.* **214**, 6 (2017).
- [42] A. W. Chao, *Physics of Collective Beam Instabilities in High Energy Accelerators* (Wiley, New York, 1993).
- [43] C. B. Schroeder Ph.D. thesis, University of California, Berkeley, 1999.